Mode transitions in nonlinear evolution of the electron drift instability in a 2D annular E × B system

Cite as: Phys. Plasmas **27**, 022309 (2020); https://doi.org/10.1063/1.5139035
Submitted: 17 November 2019 . Accepted: 24 January 2020 . Published Online: 12 February 2020

M. Sengupta, and A. Smolyakov

Physics of Plasmas ARTICLE scitation.org/journal/php

Mode transitions in nonlinear evolution of the electron drift instability in a 2D annular E × B system

Cite as: Phys. Plasmas **27**, 022309 (2020); doi: 10.1063/1.5139035
Submitted: 17 November 2019 · Accepted: 24 January 2020 ·
Published Online: 12 February 2020

M. Sengupta and A. Smolyakov

AFFILIATIONS

Department of Physics and Engineering Physics, University of Saskatchewan, Saskatoon S7N5E2, Canada

ABSTRACT

Nonlinear development of electron drift instability is studied using 2D3V azimuthal-radial Particle-in-Cell simulations of an annular Hall thruster channel of 10 cm diameter. The full 2π azimuthal domain of the annular cross section is simulated with reflecting boundary conditions at the radial boundaries. It is shown that the instability, which starts as a short length scale linear instability, undergoes a sequence of nonlinear transitions into longer wavelength modes. The transitions in the mode wavelengths are accompanied by related transitions of the magnitude of anomalous axial current. In the nonlinear stages, there is evidence of azimuthal trapping and dragging of ions by the propagating wave resulting in saturation of instability. It is demonstrated that the size of the azimuthal domain influences mode dynamics and, thereby, the anomalous cross field electron transport.

I. INTRODUCTION

The electron drift instability (EDI) is a common phenomenon in plasma systems that are classified as partially magnetized **E** × **B** plasma.[1–3] In such systems, electrons drift under a crossed electric **E** and magnetic field **B**, while ions remain unmagnetized owing to their large Larmor radius compared to the system dimensions. The unmagnetized ions are accelerated by **E** across **B** while the magnetized electrons are constrained to drift in the **E** × **B** direction. This configuration finds application in space propulsion devices,[3–5] magnetron devices used in material processing,[6] and magnetic filters used in negative ion sources,[7] and also appears in Penning discharge experiments.[8,9] The partially magnetized **E** × **B** configuration is also set up naturally in the collisionless shock waves in space conditions.[10–12]

The free energy for the growth of the EDI originates from the differential drift between the electron and ion component, due to the **E** × **B** streaming of magnetized electrons with respect to unmagnetized ions.[2,13,14] Differential drift may also occur due to the difference in collisionality of two components (as in collisional Simon–Hoh instability[15–17]) or from the differential rotation of ions and electrons in strongly rotating configurations in non-neutral plasmas.[18,19]

Operation of propulsion devices and ion sources is based on the principle that electrons are held in place by the magnetic field, allowing ions to be extracted and propelled by the electric field.[3] Plasma instabilities, such as EDI, produce fluctuating electrostatic fields resulting in drift-transport of electrons across the magnetic field **B** and along the applied electric field **E**, thus reducing the confining effects of the magnetic field on the electrons.[20,21] The increased mobility of electrons along the externally applied electric field is much higher than the mobility expected from classical electron scattering and, hence, termed anomalous electron mobility.

Understanding the nature of the anomalous electron mobility is an important problem of the E × B devices, in particular, the Hall thrusters. The EDI has been suggested as a source of plasma fluctuations that would lead to enhanced electron transport[3,14,22,23] and has been actively studied using 1D and 2D numerical simulations. Many of such simulations were done in Cartesian geometry with a limited span of 1–2 cm in the (periodic) azimuthal direction based on the assumption that the most unstable modes have the wavelength of the order of millimeters.[13,20,24–32] These numerical models have all demonstrated substantially enhanced cross field transport of electrons over classical collisional diffusion, and presented strong evidence for the EDI being the potent source of anomalous electron transport in a Hall thruster.

Some analytical and numerical models also focus on the possibility that the EDI evolves nonlinearly to the ion sound mode.[13,33,34] Recent simulations of EDI in 1D and 2D indicate that the nonlinear development of the instability causes energy flow to large length scales, resulting in the appearance of large scale (up to the simulation box size) coherent nonlinear structures.[26,27] The cascade of energy to long length scales has also been observed in recent modeling of fluid

instabilities in the Hall thruster configuration[35] and in the Hall thruster experiment.[36,37] Therefore, it is important to perform simulations of the Hall thruster using an azimuthal domain that accommodates nonlinear mode transformations up to the full azimuthal length of the device. This is one of the goals of this work.

Cartesian-box simulations do not take into consideration the role played by device curvature and divergence in the radial magnetic field of the annular Hall thruster channel. Effects, such as centrifugal forces on rotating electrons and radial variation of the magnetic field in the thruster channel, can affect the radial and azimuthal wave structure and the resulting anomalous transport.[38]

In the numerical experiments of this paper, 2D3V Particle-in-Cell (PIC) radial-azimuthal simulations are performed in the entire annular cross section of a Hall thruster to investigate the nonlinear transitions and anomalous transport. Effects of curvature and diverging magnetic field of the Hall thruster are thus naturally included in the simulations. The radial wall boundaries are maintained grounded with specular particle reflection. Effects of particle absorption and plasma sheath formation near the annular walls are not included in this model. Simplification of the mirror reflection of particles from the walls and fixed (grounded) wall potential allows focusing on the internal nonlinear dynamics of the instability without complications of the plasma sheath and additional effects due to ambipolar field that might occur for a floating wall. The linear theory predicts that the transition to the ion sound regime occurs for sufficiently large values of the radial wave-vector[1,34,39] along the magnetic field. Our model permits self-consistent linear and nonlinear development of the radial structure of the eigenmodes. One of the goals of this paper is to investigate the radial mode structure and its effect on the possible transition to the ion-sound regime.

The numerical experiments are performed for three ion species: xenon, argon, and hydrogen to investigate the ion mass effects. The effects of the magnetic field are fully retained in ion dynamics.

The simulations of this paper have revealed that EDI in the annular plasma profile evolves through a series of mode and mobility transitions. An inverse cascade process increases the azimuthal wavelength in discrete steps by a full order of magnitude from its initial value. Radial wave structures emerge in the nonlinear phase of the instability and undergo their own transitions to evolve into a sheared radial profile that is evidently strongly influenced by centrifugal forces on the rotating electrons. The measured anomalous electron mobility makes transitions correlated with the azimuthal structure of the eigenmodes, by evolving from a linearly growing phase, to a quasi-stationary phase, and to a nonlinear evolution to saturation. During the nonlinear transitions, some ions are trapped and dragged along by the propagating mode, leading to saturation of the instability. The focus of the paper is on numerical modeling of the transitional dynamics and investigating how these collisionless processes scale with variation of the ion mass.

In the linear analyisis, EDI is well understood as the Electron Cyclotron Drift instability (ECDI)[1,2] and has been referred to as such in parts of the paper, where the linear form of the instability is indicated (mainly Sec. II). In the rest of the paper, when referring to nonlinear dynamics and transport, the term Electron Drift instability (EDI) is used.

In Sec. II, some background information on the theory of ECDI is presented. Section III describes the details of the numerical setup of the simulations. EDI mode transitions in xenon plasma, and its comparison with the lighter argon and hydrogen plasmas make up Subsections IV A and IV B of Sec. IV. A supplementary experiment to understand the role of the system size in the evolution of the instability, and some numerical convergence tests are also presented in Subsection IV B of Sec. IV. The final Sec. V presents a summary of the results.

II. ECDI: A LINEAR MODEL

In this work, PIC simulation is used to model the kinetic electron drift instability in an annular configuration of the $\mathbf{E}\times\mathbf{B}$ plasma. It is therefore useful to briefly consider the results from existing linear theory of this instability in slab geometry. As mentioned earlier, in its linear analytical model, the instability is called as Electron Cyclotron drift instability or ECDI.

Consider a uniform, partially magnetized, $\mathbf{E}\times\mathbf{B}$ plasma configuration with crossed electric and magnetic fields: $\mathbf{E}=E\mathbf{x}$, $\mathbf{B}=B\mathbf{z}$, so that the electron drift velocity, $\mathbf{v_d}=-v_d\mathbf{y}=\mathbf{E}\times\mathbf{B}/B^2=-(E/B)\mathbf{y}$, where $\mathbf{x}$, $\mathbf{y}$, $\mathbf{z}$ are the Cartesian unit vectors. The electrons are drifting with $\mathbf{v_d}$ while the ions are unmagnetized and motionless.

Buneman had derived the cold plasma dispersion relation for the differential-drift driven fluctuations in the above system using 3D wave-vector $\boldsymbol{k}=(k_x,k_y,k_z)$ and ω, the wave angular frequency.[40] For the present numerical experiment, it is convenient to work with a reduced 2D form of this dispersion equation expressed in the laboratory frame (rest frame of ions), as shown below:[27]

$$\frac{k_y^2\omega_{pe}^2}{k^2\left[(\omega-k_yv_d)^2-\omega_{ce}^2\right]}+\frac{k_z^2\omega_{pe}^2}{k^2(\omega-k_yv_d)^2}=1-\frac{\omega_{pi}^2}{\omega^2}. \tag{1}$$

Here, ω_{pe} and ω_{pi} are the electron and ion plasma frequencies, and ω_{ce} is the electron cyclotron frequency.

The fluid reactive instability represented by the dispersion relation, Eq. (1), is known as the Modified Buneman Two Stream instability (MBTSI). For a sufficiently small value of the cross field wave vector k_y, the resulting solution of Eq. (1) is a 2D mode called the Modified Two Stream Instability (MTSI), which can be a significant source of transport and heating along the magnetic field.[41] For k_y larger than a lower cut-off value defined by resonance of the first term in Eq. (1), i.e., $(\omega-k_yv_d)^2-\omega_{ce}^2=0$, the unstable solution has a continuous spectrum in the (k_y, k_z) space between this lower cut-off and a another upper cut-off on k_y, defined by plasma parameters. Illustrative examples of MBTSI dispersion solution are available in Fig. 3 of Ref. 26.

Effects of finite electron temperature, T_e, change the instability in the kinetic regime. The dispersion relation in this case is given by Eq. (1),

$$\epsilon(\omega,\mathbf{k})=1+\epsilon_i(\omega,\mathbf{k})+\epsilon_e(\omega,\mathbf{k})=0, \tag{2}$$

$$\epsilon_i=-\frac{\omega_{pi}^2}{\omega^2}, \tag{3}$$

$$\epsilon_e=\frac{1}{k^2\lambda_D^2}Z'\left[1+\frac{\omega-\boldsymbol{k}.\boldsymbol{v_d}}{\sqrt{2}k_zv_e}\sum_{j=-\infty}^{\infty}\exp(-b)I_j(b)\times Z\left(\frac{\omega-\boldsymbol{k}.\boldsymbol{v_d}+j\omega_{ce}}{\sqrt{2}k_zv_e}\right)\right]. \tag{4}$$

Equations (2)–(4) represent the ECDI dispersion relation. Here, $b = k_y^2\rho_e^2$, $\rho_e^2 = v_e^2/\omega_{ce}^2$, $v_e = \sqrt{\frac{k_B T_e}{m_e}}$, m_e is the electron mass, λ_D is the electron Debye length given by $\lambda_D = \sqrt{\frac{\epsilon_0 k_B T_e}{n_e e^2}}$, e is the electron charge, $Z(\xi)$ is the plasma dispersion function, $I_j(x)$ represents the modified Bessel function of the first kind, and the index $j = 1, 2, 3, \ldots, \infty$ will be referred to as the resonant mode index.

As evident from the sample numerical solutions of Eqs. (2)–(4) in Fig. 1, the finite electron temperature results in unstable 2D ECDI modes due to the kinetic resonances near the conditions $(\omega - k_y v_d)^2 - j^2\omega_{ce}^2 = 0$, along with the sub-cutoff MTSI mode at small k_y. The modes primarily propagate in the cross field, i.e., k_y direction, and get coupled in the parallel direction with a relatively smaller k_z. The influence of k_z on the ECDI + MTSI dispersion spectrum (Fig. 1) is that at higher k_z and/or higher electron temperatures the sharp ECDI resonances spread out and merge into one another, tending toward an ion sound dispersion solution.[1,34,39]

For ECDI modes for the typical Hall thruster parameters, the frequencies of the resonant modes at $j \geq 1$ are such that $\omega \ll k_y v_d \approx j\omega_{ce}$ and hence, their resonance conditions may be approximated as $k_y v_d \approx j\omega_{ce}$. This resonance condition can be expressed in cylindrical co-ordinates of the annular thruster as $n\Omega \approx j\omega_{ce}$, where n is the azimuthal mode number, and Ω is the rigid angular velocity of electron drift in the annular channel, expressed as $\Omega = E_z/(r\,B(r))$. Here, E_z is the constant axial electric field, and the term $(r\,B(r))$ is also a constant, as $B(r)$ is the value of the radial magnetic field at radius r.

As the ECDI dispersion Eqs. (2)–(4) is in slab geometry, it is meaningful to obtain a set of local solutions in the annular channel (Fig. 2) at different radii, to account for the radial variation in the ω_{ce} that is used in Eqs. (2)–(4). Figure 1 is a set of graphical solutions[27,34] for the growth rate α from Eqs. (2)–(4) obtained for values of ω_{ce} at different radial locations, viz., the inner wall, the mean radius, and the outer wall. The solutions are for a xenon plasma at an electron temperature of 10 eV. A constant value of k_z (equivalent to k_r in the annular configuration) is used in the solution that corresponds to a wavelength twice the radial width of the thruster channel. The choice of electron temperature and radial wave vector used in the solution Fig. 1 roughly corresponds to the early linear phase of the Xe-thruster simulation, as will be explained in Sec. IV.

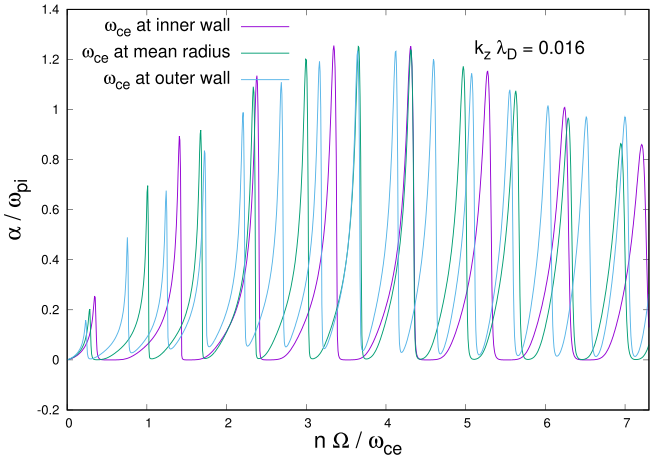

FIG. 1. The growth rate from 2D Cartesian ECDI dispersion at $T_e = 10$ eV and (i) $\omega_{ce} = 2.638 \times 10^9$ rad/s, the value at inner radial wall, (ii) $\omega_{ce} = 2.173 \times 10^9$ rad/s, the value at the mean radius of the annular channel, (iii) $\omega_{ce} = 1.847 \times 10^9$ rad/s, at the outer radial wall. α is the linear growth rate and ω_{pi} is the ion oscillation frequency. Debye length $\lambda_D = 74.3\,\mu$m and $k_z = 209.44$ rad m^{-1}, n is the azimuthal mode number and Ω is the rigid rotational velocity of electron drift in the annular channel.

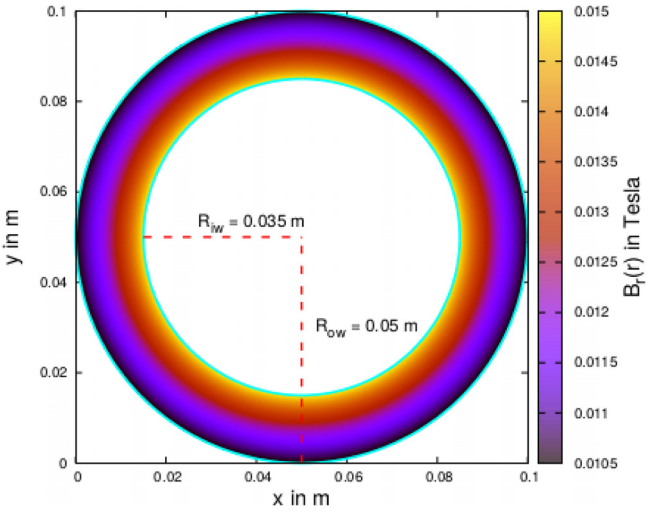

FIG. 2. Diagram of the 2D simulation region, 0.1 m × 0.1 m. The color coding depicts the topology of the radial magnetic field in the annular channel. R_{iW} and R_{oW} are the radii of the inner and outer reflecting wall, respectively.

III. THE NUMERICAL SETUP

The numerical experiments in this paper have been performed using the 2D3V Electrostatic PIC code PEC2PIC developed by Sengupta and Ganesh.[42] PEC2PIC is short for Parallelized Electrostatic Cartesian 2D Particle-In-Cell code. The key operational features of the code include Open Multi-Processing (Open-MP) parallelization, Cartesian grid, cumulative density inversion method for initial loading of plasma,[43,44] first order Cloud-in-Cell (CIC) scheme[42,43] for charge distribution on grid and a corresponding first order $(CIC)^{-1}$ scheme for field interpolation from grid to particle position,[42,43] a red–black parallelized Successive-Over-Relaxation (SOR) Poisson Solver, and a first order Chin's exponential splitting scheme as the numerical integrator for moving particles.[45] Detailed description of these numerical methods can be found in earlier works and references therein.[42,46] Multiple numerical benchmarks of PEC2PIC were demonstrated in device simulation of Penning–Malmberg trap experiments.[19,42,46–49]

The essential modifications and integration of new features in PEC2PIC for simulation of the annular thruster cross section are explained below.

A. Specular particle reflections from the walls

In the current model, physical sources and sinks for electron and ions that exist in a real thruster system are not included in the simulation. In line with this simplification, is the use of perfectly reflecting radial walls to keep the loaded particles confined through the

simulation. The algorithm adapted to execute radial wall reflections is as follows.

In a given simulation time step, a particle that overshoots a radial boundary with fixed time step velocity $\mathbf{v}$ is back traced in time checking its radius at every point. As soon as the particle's radius hits the wall radius value, the back trace is stopped. At this radius and corresponding azimuthal angle, the cylindrical components of the velocity v are obtained through transformation of the Cartesian velocity components. Now, only the radial component of $\mathbf{v}$ is reversed and the modified cylindrical velocity components are transformed back to Cartesian to yield a reflection modified velocity $\mathbf{v}_{rm}$. The particle is then moved forward in time with $\mathbf{v}_{rm}$ for the same length of time it was back traced. This procedure implements specular particle reflections on the inner and outer radial walls of the device.

B. Virtual axial domain

In these simulations, the Poisson equation is solved in the 2D (x, y) plane, while the third direction, along the axis of the discharge, is not resolved. In Hall thruster devices, anomalous electron transport and ion propulsion result in continuous removal of heated/accelerated particles and their replacement with "fresh" cold particles. It has been proposed by Boeuf[50] to mimic this effect using a virtual finite length axis in the simulation. The application of the virtual axial domain following Boeuf's procedure is outlined below.

The particles are loaded cold, i.e., with zero velocities and to each is assigned an initial axial position uniformly distributed through the thruster channel's axial length of 1 cm. The axial positions are updated in every time step of the 2D3V simulation. If a particle crosses any one axial end of the channel in a given time step, it is re-introduced cyclically through the opposite end as a fresh cold particle. The procedure can also be described as a replacement of energetic particles with cold particles thus restraining particle heating. Note that the particle's position on the PIC plane remains unaltered by the process, keeping the planar simulation free of any spurious phase mixing.

C. Numerical integration for Cartesian mesh with diverging magnetic field in the simulation plane

A planar Cartesian decomposition of the radially divergent magnetic field, $\mathbf{B_r}$ acting on particle p at time t, is a function of the cylindrical polar co-ordinates of the particle, $r_p(t)$ and $\theta_p(t)$. Any particle pusher defined on the Cartesian mesh will have to be adapted to include this functional dependence of the Cartesian magnetic field components on the cylindrical polar co-ordinates. To demonstrate how this adaptation was implemented in PEC2PIC, the general form of the numerical integrator as derived by Chin is first concisely presented in Eqs. (5)–(10), and then, the adapted form of the integrator for the Hall thruster topology is expressed in Eq. (11).

Consider a charged particle of charge q and mass m with position and velocity vectors $\mathbf{x}$ and $\mathbf{v}$ in an electric field $\mathbf{E}(\mathbf{x})$ plus a magnetic field $\mathbf{B}(\mathbf{x})$. The equations of motion for this system are[42]

$$\mathrm{m}\frac{d\mathbf{v}}{dt} = \mathrm{q}\left[\mathbf{v}\times\mathbf{B}(\mathbf{x}) + \mathbf{E}(\mathbf{x})\right]. \tag{5}$$

From (1), the Evolution Operator of this system can be obtained as $e^{t(\mathcal{T}+\mathcal{V}_{BF})}$, where[42]

$$\mathcal{T} = \mathbf{v}\cdot\nabla_x, \quad \mathcal{V}_{BF} = \left[-\frac{\mathrm{q}B(\mathbf{x})}{\mathrm{m}}\hat{\mathbf{B}}(\mathbf{x})\times\mathbf{v} + \frac{\mathrm{q}}{\mathrm{m}}\mathbf{E}(\mathbf{x})\right]\cdot\nabla_v. \tag{6}$$

Now, the first component of the evolution operator $e^{t\mathcal{T}}$ is the translation operator, which operates simply as[42]

$$e^{t\mathcal{T}}\begin{pmatrix}\mathbf{x}\\ \mathbf{v}\end{pmatrix} = \begin{pmatrix}\mathbf{x}+t\mathbf{v}\\ \mathbf{v}\end{pmatrix}. \tag{7}$$

The operation of the second component, $e^{t\mathcal{V}_{BF}}$, can be shown to be[42]

$$e^{t\mathcal{V}_{BF}}\begin{pmatrix}\mathbf{x}\\ \mathbf{v}\end{pmatrix} = \begin{pmatrix}\mathbf{x}\\ \mathbf{v}_B(\mathbf{x},\mathbf{v},t)+\mathbf{v}_F(\mathbf{x},t)\end{pmatrix}$$

where

$$\mathbf{v}_B(\mathbf{x},\mathbf{v},t) = \big[\mathbf{v} + \sin(\theta(\mathbf{x},t))(\hat{\mathbf{B}}(\mathbf{x})\times\mathbf{v}) + (1-\cos(\theta(\mathbf{x},t)))\{\hat{\mathbf{B}}(\mathbf{x})\times(\hat{\mathbf{B}}(\mathbf{x})\times\mathbf{v})\}\big]$$

and

$$\mathbf{v}_F(\mathbf{x},t) = \left[t\frac{\mathrm{q}}{\mathrm{m}}\mathbf{E}(\mathbf{x}) + \frac{t}{\theta(\mathbf{x},t)}\left(\hat{\mathbf{B}}(\mathbf{x})\times\frac{\mathrm{q}}{\mathrm{m}}\mathbf{E}(\mathbf{x})\right)\times(1-\cos(\theta(\mathbf{x},t))) + t\left(\hat{\mathbf{B}}(\mathbf{x})\times\left(\hat{\mathbf{B}}(\mathbf{x})\times\frac{\mathrm{q}}{\mathrm{m}}\mathbf{E}(\mathbf{x})\right)\right)\left(1-\frac{\sin(\theta(\mathbf{x},t))}{\theta(\mathbf{x},t)}\right)\right]$$

and,

$$\theta(\mathbf{x},t) = -(t\mathrm{q}B)/\mathrm{m}. \tag{8}$$

Equations (7) and (8) represent operation of the components of the evolution operator, $e^{t\mathcal{T}}$, and $e^{t\mathcal{V}_{BF}}$ in a closed form.[45] Now using the exponential splitting technique in Eq. (9), the numerical integrator of any $(\mathcal{M}+1)$ order may be obtained as shown below:[42,45]

$$e^{t(\mathcal{T}+\mathcal{V}_{BF})} = \prod_{l=0}^{\mathcal{M}} e^{td_l(\mathcal{T})}\, e^{tc_l(\mathcal{V}_{BF})} + \mathcal{O}(t^{\mathcal{M}+2}). \tag{9}$$

Here, c_l and d_l are constant coefficients to be determined by exponential series expansion of Eq. (9). Putting $\mathcal{M}=0$ gives a first order approximation $e^{t(\mathcal{T}+\mathcal{V}_{BF})} \approx e^{td_0(\mathcal{T})}\, e^{tc_0(\mathcal{V}_{BF})}$ which yields $d_0 = c_0 = 1$. The resultant first order integrator is expressed in vector as well as component form in Eq. (10):

$$\begin{aligned}
&\mathbf{v}_1 = \mathbf{v}_B(\mathbf{x}_0,\mathbf{v}_0,\Delta t) + \mathbf{v}_F(\mathbf{x}_0,\mathbf{v}_0,\Delta t)\\
\Rightarrow\ &v_{1i} = v_{Bi}(\mathbf{x}_0,\mathbf{v}_0,\Delta t) + v_{Fi}(\mathbf{x}_0,\mathbf{v}_0,\Delta t)\\
&\mathbf{x}_1 = \mathbf{x}_0 + \Delta t\,\mathbf{v}_1\\
\Rightarrow\ &x_{1i} = x_{0i} + \Delta t\, v_{1i}\\
&\text{where, } (\mathbf{x}_0\,\mathbf{v}_0) \text{ is transformed to} (\mathbf{x}_1\,\mathbf{v}_1) \text{ in time} - \text{step } \Delta t,\\
&i = 1,2,3 \text{ are Cartesian components.}
\end{aligned} \tag{10}$$

The adaptation of the Cartesian-decomposed, first-order exponential splitter, Eq. (10), for a radially diverging magnetic field, $B_r = B_0\, R_{iw}/r$, is expressed in Eq. (11):

$$v_{x1} = v_{x0} + v_{z0}\sin\psi\sin\theta + (1-\cos\theta)(v_{y0}\cos\psi\sin\psi - v_{x0}\sin^2\psi) + \Delta t\frac{q}{m}E_x + \frac{\Delta t}{\theta}(1-\cos\theta)\frac{q}{m}E_z\sin\psi$$
$$+\Delta t\left(1-\frac{\sin\theta}{\theta}\right)\frac{q}{m}(E_y\cos\psi\sin\psi - E_x\sin^2\psi)$$
$$v_{y1} = v_{y0} - v_{z0}\cos\psi\sin\theta - (1-\cos\theta)(v_{y0}\cos^2\psi - v_{x0}\sin\psi\sin\psi) + \Delta t\frac{q}{m}E_y - \frac{\Delta t}{\theta}(1-\cos\theta)\frac{q}{m}E_z\cos\psi$$
$$-\Delta t\left(1-\frac{\sin\theta}{\theta}\right)\frac{q}{m}(-E_y\cos^2\psi + E_x\cos\psi\sin\psi)$$
$$v_{z1} = v_{z0} + (v_{y0}\cos\psi - v_{x0}\sin\psi)\sin\theta - v_{z0}(1-\cos\theta) + \Delta t\frac{q}{m}E_z + \frac{\Delta t}{\theta}(1-\cos\theta)\frac{q}{m}(E_y\cos\psi - E_x\sin\psi) - \Delta t\left(1-\frac{\sin\theta}{\theta}\right)\frac{q}{m}E_z$$
$$\text{where,}\quad \sin\psi = (y_0-y_c)/r_0\,,\ \cos\psi = (x_0-x_c)/r_0\,,$$
$$r_0 = \sqrt{(x_0-x_c)^2+(y_0-y_c)^2}\quad\text{and,}\quad \sin\theta = \frac{\Delta t q B_0 R_{iw}}{m r_0}\quad\text{and then,}$$
$$x_1 = x_0 + v_{x1}\Delta t$$
$$y_1 = y_0 + v_{y1}\Delta t. \tag{11}$$

D. Parameters of simulations

The simulations are performed on the Cartesian grid, covering the annular channel such as shown in Fig. 2. The dimensions of the outer box are $0.1\,\text{m} \times 0.1\,\text{m}$. The box is uniformly meshed by 700×700 Cartesian PIC cells.

These outer and inner circular boundaries have radii $R_{ow} = 0.05\,\text{m}$ and $R_{iw} = 0.035\,\text{m}$, respectively. As shown in Fig. 2, the radial magnetic field B_r falls as $1/r$ from $0.015\,T$ to $0.0105\,T$ between the inner and outer radial walls. The annulus is initially filled with a cold (zero-velocity) plasma with the uniform density $n_e = n_i = 1.0 \times 10^{17}\,\text{m}^{-3}$. The radial boundaries are specularly reflecting for particles, so there is neither any sheath here, nor plasma losses.

Crossed electric and magnetic fields are applied externally in the cavity to produce the $E \times B$ plasma. The radial magnetic field falls with the radius r, as $B_r = B_0 R_{iw}/r$, where $B_0 = 0.015\,T$, and the applied uniform axial electric field out of the simulation plane is $E_z = 2 \times 10^4\,\text{V/m}$. This gives the value of the rigid angular drift velocity of electrons to be $\Omega = E_z/(B_0 R_{iw}) = 3.8095 \times 10^7\,\text{rad/s}$.

The electron and ion components are represented by 2.5×10^6 superparticles distributed as 13 particles-per-cell in the annular channel. Convergence test simulations are also performed with ppc = 30, 60 that show a similar result (see Figs. 19–21). Both species are moved with the same simulation time-steps, $\Delta t = 5 \times 10^{-12}\,\text{s}$. This $\Delta t = 5 \times 10^{-12}\,\text{s}$ resolves the smallest electron cyclotron time in the annular channel, $T_{ce} = 2.382 \times 10^{-9}\,\text{s}$ as well as the electron oscillation time, $T_{pe} = 3.522 \times 10^{-10}\,\text{s}$.

The shortest wavelength mode is excited in course of the simulations, with an azimuthal mode number $n = 246$ corresponding to the wavelength of around 1 mm. The milli-metre length scale of this mode[26,27,51] is an order longer than the Debye length $\lambda_D = 0.074\,\text{mm}$ at the linear phase temperature of 10 eV. As is discussed in more detail below in Sec. IV, the linear excited mode corresponds to the cyclotron resonance condition $(n\Omega/\omega_{ce}) = 3 - 5$. The 700×700 mesh used in the simulation has a resolution of $\Delta x = 0.14\,\text{mm}$ that finely resolves the shortest wave structure, but not the Debye length. Hence, it is necessary to consider the possibility and extent of numerical grid heating in the simulation. This is done with the help of a test simulation outlined below.

A supplementary simulation is performed on the 700×700 mesh for a half-sized (5 cm diameter) device with a grid resolution of $\Delta x = 0.07\,\text{mm}$. The objective is to demonstrate the global effect of the system size on nonlinear saturation of the EDI at long wavelengths. Divergence between 10 cm and 5 cm device simulations in the saturation stage of the instability is indicative of this effect. However, in the linear phase, when the mode wavelength (1 mm) is too small to be affected by the system size, the two simulations are equivalent, except for the fact that the 5 cm device is simulated on a grid of twice finer resolution, $\Delta x = 0.07\,\text{mm}$, which is even shorter than the linear phase Debye length of 0.074 mm. A fairly good linear phase convergence is obtained between the two simulations, which indicates that the plasma evolution on the $\Delta x = 0.14\,\text{mm}$ mesh is not significantly deviated by numerical grid heating. A possible explanation for this is that the electron heating in the system is substantially controlled by the continuous cold reinjection of lost electrons in the virtual axial domain. That being said, there is still an initial jump in the electron temperature from zero to 10 eV observed in the 10 cm device simulation on the $\Delta x = 0.14\,\text{mm}$ mesh. This jump happens at a very fast time scale of around $0.01\,\mu\text{s}$ and could be possibly due to grid heating on the initially cold plasma.

IV. LINEAR AND NONLINEAR DYNAMICS OF EDI IN THE ANNULAR CONFIGURATION

Evolution of an initially cold, xenon plasma in the annular thruster cross section is investigated in Subsection IV A. To understand how different aspects of the EDI such as the growth rate and electron transport scale with the mass of the ion species, the same numerical experiment has been conducted using two lighter ion species, that of argon and hydrogen. The lighter ion experiments are reported in Subsection IV B.

A. Evolution of EDI and anomalous electron transport in annular xenon plasma

1. Phases of the instability

From the plasma electrostatic energy plot of Fig. 3, it is evident that for Xe^+, the initial linear exponential growth of the instability, at a

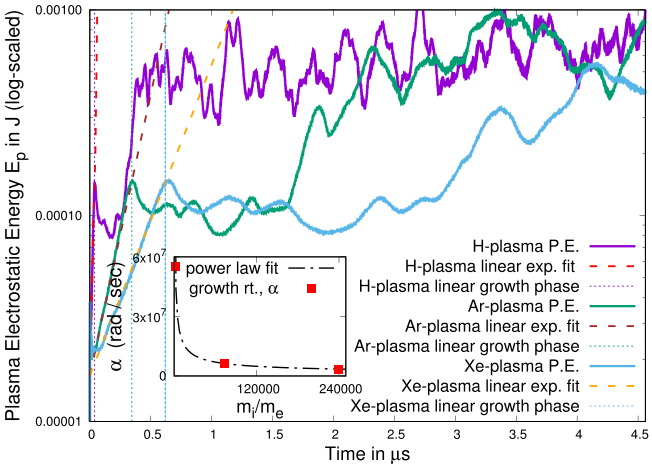

FIG. 3. Potential (logscale)energy, E_p as a function of time, t. (Inset) A power law fit of the EDI growth rate α as a function of ion-mass $\sim(m_i/m_e)^{-0.6}$.

growth rate of $\alpha = 3.48 \times 10^6$ rad/ sec, lasts up to $t = 0.62\,\mu$s. Thereafter, the instability proceeds nonlinearly in two stages: a quasi-stationary energy phase (0.62 μs to 2.5 μs), followed by a nonlinear energy transition between 2.4 μs and 4.0μs to reach another saturation near the end of the simulations at 4.55 μs.

2. Anomalous axial electron transport

The electron axial mobility μ_{ez} depicted in Fig. 4 is calculated as $(\sum_{p=1}^{\xi_e} v_{pz})/(\xi_e E_z)$, where p is the index of electron superparticles and v_{pz} is the axial component of its velocity, ξ_e is the total number electron superparticles, and E_z is the magnitude of the applied axial electric field. In these collisionless simulations, electrons are transported across the magnetic field due to the fluctuating electric field $\boldsymbol{E}_\theta$ crossed with the $\mathbf{B_r}$.[52]

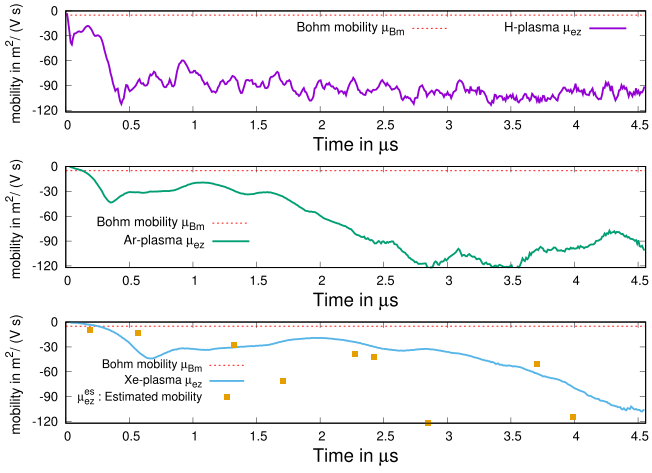

FIG. 4. Electron mobility, μ_{ez} as a function of time. As a reference the Bohm mobility, $\mu_{Bm} = 1/(16\,B_r)$ is plotted for the value magnetic field at the mean radius of the channel, $B_r = 0.01235\,T$. In the Xe-plasma subplot, the yellow dots represent the estimated value of the mobility from analytical expression μ^{es}_{ez}.

When collisional effects are negligible, the estimate for μ_{ez} can be obtained as follows $\mu^{es}_{ez} = \langle n_e E_\theta \rangle / (n_e B_r E_z)$ where superscript "es" means the estimated value, $\langle n_e E_\theta \rangle$ is the volume average of $n_e E_\theta$ in the simulation domain, while the n_e in the denominator can be taken as the initial uniform density, and B_r may be approximated by its value at the mean radius. The values of μ^{es}_{ez} have been plotted (yellow square) for a set of time-points in the Xe-plasma subplot of Fig. 4. These are instantaneous values without any smoothing in time, and, as such, they are very noisy.[13] Nevertheless, there is reasonable agreement between the directly measured and estimated values of the cross field mobility, with the latter roughly showing the transitional characteristics of the experimental μ_{ez} curve. The transition of the mobility to larger values in the nonlinear stages of the instability indicates the strengthening of the negative correlation between n_e and E_θ by the inverse cascade of azimuthal structures.

In the xenon plasma subplot of Fig. 4, the μ_{ez} shows distinct transitions in the three phases of the instability. In the linear phase, there is a linear exponential growth of μ_{ez} from zero to a magnitude of about 45 $\mathrm{m^2\,V^{-1}\,s^{-1}}$. Thereafter in the quasi-stationary energy phase, the magnitude of μ_{ez} remains stable. Again in the nonlinear energy transition phase, the μ_{ez} curve also makes a nonlinear transition to saturate at a value around 115 $\mathrm{m^2\,V^{-1}\,s^{-1}}$.

The anomalous electron mobility values obtained from these radial-azimuthal simulations are higher than the corresponding values obtained from 1D and 2D Cartesian box simulations in similar parametric conditions,[13,26,27,29] by roughly half an order of magnitude. The availability of the full 2π *rad* azimuthal domain allows the EDI modes to nonlinearly cascade to longer wavelengths compared to smaller periodic domain simulations. The transition to longer wavelength enhances the anomalous electron transport. A verification of this hypothesis is demonstrated later in Subsection IV B with the help of a hydrogen plasma simulation on a reduced azimuthal domain.

Another reference point of interest in the mobility curve is the Bohm mobility $\mu_{Bm} = (16B_r)^{-1}$ plotted as a dashed red line in Fig. 4. The value of μ_{Bm} has been obtained using the B_r at the mean radius of the channel. The anomalous transport due to large scale structures created by the inverse cascade in the full sized azimuthal domain takes the anomalous mobility to values as high as 20 times the Bohm mobility in the course of simulation. The transition of mobility to such large magnitudes has also been verified with convergence tests performed with higher particles-per-cell in Subsection IV B. Mobility in other collisionless PIC simulations (or collisional simulations at sufficiently low pressures) in much smaller azimuthal domains,[13,53] as well as corresponding estimates from $\langle n_e E_\theta \rangle$ fed from the same simulations also give values that are two to –three times larger than Bohm mobility. At this time, we do not have a clear explanation for these observations. It is plausible that anomalous transport is generally overestimated due to the absence of some stabilizing and loss mechanisms that are present in real discharges, e.g., due to sheath losses. We also note that the turbulent transport does not conform to the $1/B$ scaling and that some experimental studies have also measured turbulent collisionless transport in the thruster channel as large as 10 times that expected from Bohm transport,[54,55] whereas other experimental studies[56] and simulations[27,57] suggest that effective mobility should be less than or equal to the Bohm value.

The collisional effects of electron scattering against the radial walls, and the axial replacement of energetic electrons by cold electrons

which are in effect inelastic collisions, are determined to be inconsequential in the transport process. In Fig. 5, a sample electron from the Xe-plasma simulation undergoes 68 reflections between the radial walls in an interval of 0.76 μs, and in the same interval its virtual axial displacement counter gets reset 53 times after traversing the virtual channel length. These collision statistics give a net electron collision frequency, $\nu = 1.59 \times 10^8\ s^{-1}$. Substituting this ν and the ω_{ce} at mean radius of the channel, in the collisional (classical) axial mobility expression, $\mu_{ez}^{col} = \frac{e/(m\nu)}{[1+\omega_{ce}^2/\nu^2]}$, its value can be estimated to be, $\mu_{ez}^{col} = 5.893\ m^2\ V^{-1}\ s^{-1}$. This is insignificant compared to the values of μ_{ez} measured in Fig. 4.

3. Electron heating

Figure 6 demonstrates the evolution of electron 1D temperatures in θ, r, and z over the simulation period. For the Xe-plasma, there is a jump in the electron 1D temperatures from zero to around 10 eV at a very fast time scale of about 0.01 μs.It is hypothesized that the quick jump of electron temperature from $T_e = 0$ to $T_e = 10$ eV could be a combination of grid heating (more effective in the initial cold plasma), and radial profile relaxation through bounce motion of electrons between the curved reflecting surfaces. The bounce time of electrons in the annular channel with a typical radial velocity of 2.0×10^6 m/s is in the same ballpark as the temperature ramp up time of 0.01 μs.

After the initial temperature jump, a smooth linear exponential growth to 25 eV is observed in Fig. 6—Xe^+ subplot. This is primarily due to the collisionless heating by the linearly growing EDI mode. With the transition to the nonlinear phase, and the continuous process of cold particle re-injection, the electron 1D temperatures saturate around the 25 eV mark.

A set of energy distributions at different points of time post temperature saturation is plotted in Fig. 7. The electron distribution is near-Maxwellian except at very low energies where there is a peak of electrons that have undergone axial replacement cooling around that point of time. The ion distribution curves have similar features at very low energies for the same reason. Beyond the low energy distribution,

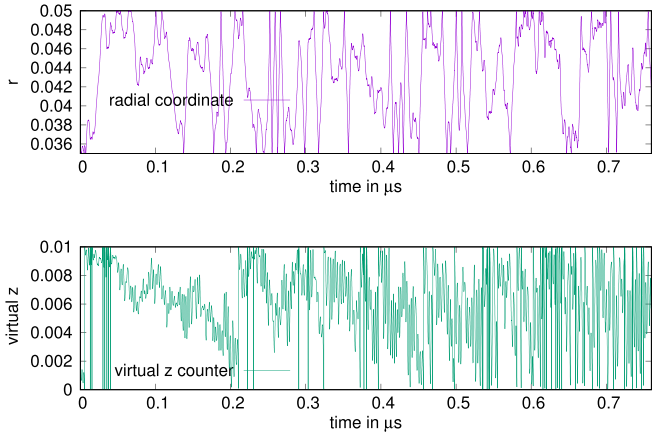

FIG. 5. Estimation of electron collision frequencies in Xe-plasma using an electron's trajectory in the 0.76 μs interval between $t = 0.76$ μs and $t = 1.52$ μs. (top) The radial trajectory in the interval measures 68 wall reflections. (bottom) The virtual z counter gets re-set to 53 times in the interval.

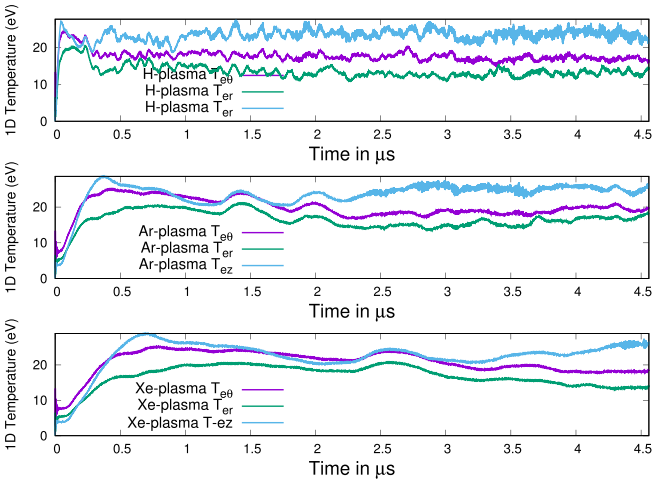

FIG. 6. Radial, (T_{er}), azimuthal ($T_{e\theta}$), and axial (T_{ez}) electron temperatures as a function of time.

the ion energy distributions have a non-Maxwellian bell shape. The small peak in the tail of the ion distribution observed around 200 eV is formed by the axially extracted ions in the propulsion device.

4. Azimuthal mode transitions

Figure 8 is a set of time-frames of the normalized Xe^+ density in an arbitrary polar section of the simulated device. The full annular profile of the normalized Xe^+ density is also shown for selected few time-frames in Fig. 9. Together Figs. 8 and 9 are the visual representation of the linear and nonlinear dynamics of the excited 2D modes in the plasma. In Fig. 8, the first four snapshots ($t = 0.0095$ μs to 0.5795 μs) belong to the linear growth phase, snapshots 5–8 ($t = 0.7695$ μs to 2.0995 μs) are in the quasi-stationary energy phase, while snapshots 9–12 ($t = 2.8595$ μs to $t = 4.5505$ μs) are in the nonlinear energy transition phase. In Fig. 9, the first snapshot is in the

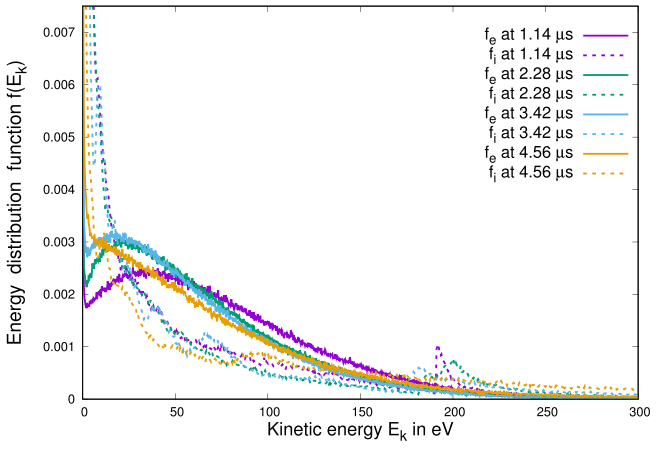

FIG. 7. Energy distribution functions for electrons, f_e and ions, f_i at different stages of the Xe-plasma simulation. E_k is the particle kinetic energy.

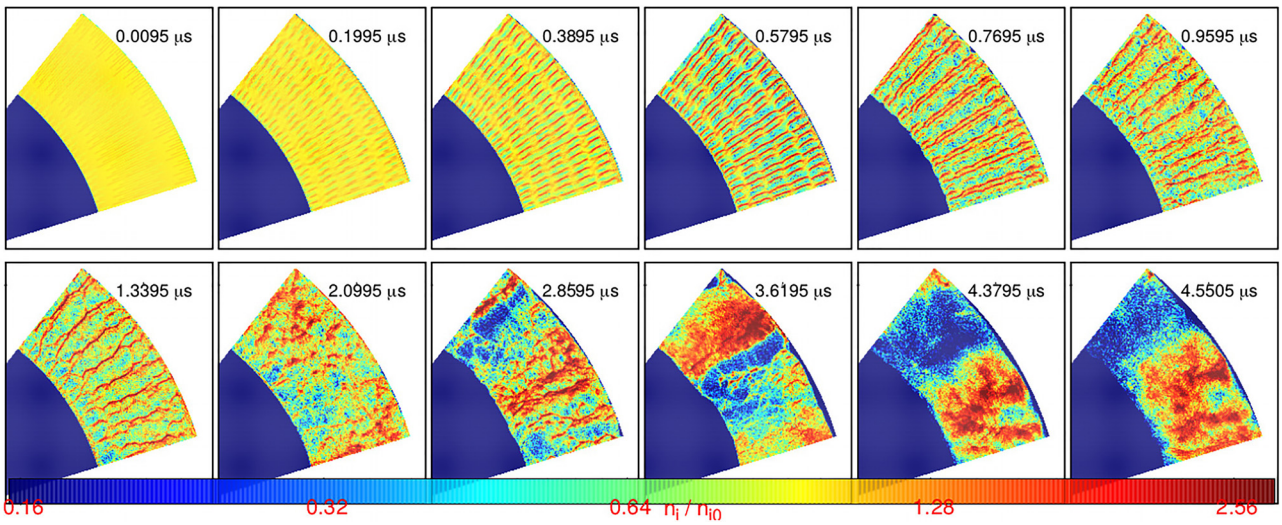

FIG. 8. The evolution of the ion density, for xenon plasma. The same azimuthal segment of the annular device is shown at selected time frames. The n_i color bar is logscaled and normalized by the initial value n_{i0}.

linear growth phase, the second and third are in the quasi-stationary phase, and the fourth is in the nonlinear energy transition phase.

In Fig. 10, the 2D annular Xe^+ density profile is first radially averaged, and then scanned for excited azimuthal modes with the azimuthal FFT operation. Three stacked subplots in each time-frame of Fig. 10 depict the ion density function in full 2π domain (top), a zoomed-in depiction of the same density function on a smaller azimuthal angular domain (middle), and angular FFT of the density function in the 2π domain (bottom). The time frames chosen are the same as in Fig. 8. In the linear stage [Figs. 10(a)–10(d)], the azimuthal profile has a growing $n = 246$ mode, whose linear growth rate extracted from Fig. 3 is $\alpha = 3.48 \times 10^6$ rad/s. The linear phase dynamics in the annular profile agrees well with the dispersion analysis of the ECDI in 2D Cartesian geometry, Fig. 1, as explained below.

The plateau profile of the radial density function in the linear stage [see Figs. 11(a)–11(c)], approximately forms half a wave in the radial width of the channel. Such a half-wave in the direction parallel to the magnetic field has also been observed in a Cartesian box simulation using dielectric radial boundaries.[27] In the dispersion analysis of Fig. 1, the value of the radial wave vector used is, $kz = 209.44\ \mathrm{rad\,m^{-1}}$ (k_z of Fig. 1 is equivalent to the k_r in the cylindrical system). This k_z represents a radial wave having wavelength twice the radial width of the channel. Again, as linear growth of the $n = 246$ commences after the initial electron temperature jump to 10 eV, the value of T_e used in Fig. 1 is also 10 eV.The three curves in Fig. 1 represent the EDI dispersion at the three values of ω_{ce}, corresponding to the inner wall radius, mean radius, and the outer wall radius of the channel.

For the dispersion relation at the inner wall radius, the most powerful resonance peak is around $(n\Omega/\omega_{ce}) = 3$, i.e., $n = 208$ and resonance index $j = 3$. In the spectrum of the dispersion relation at the mean radius, the second most powerful resonance is around $(n\Omega/\omega_{ce}) = 4$, i.e., $n = 228$ and $j = 4$. The solution at the outer wall radius has the third highest peak around $(n\Omega/\omega_{ce}) = 5$, i.e., $n = 242$ and $j = 5$. The linearly growing azimuthal mode from simulation, $n = 246$, falls inside the width of these particular, maximum or near-maximum resonant peaks of the solutions in Fig. 1. This observation intuitively explains why the EDI excites $n = 246$ on the annular profile. Furthermore, the growth rates at $(n\Omega/\omega_{ce}) = 3$, $(n\Omega/\omega_{ce}) = 4$, and

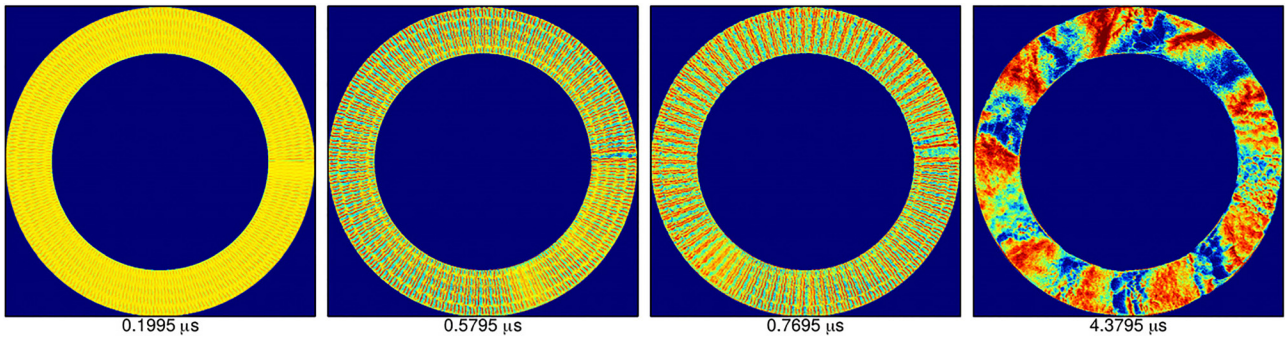

FIG. 9. The evolution of the ion density, for xenon plasma. Selected time frames of the full annular device are shown. Normalization and color scheme are the same as in Fig. 8.

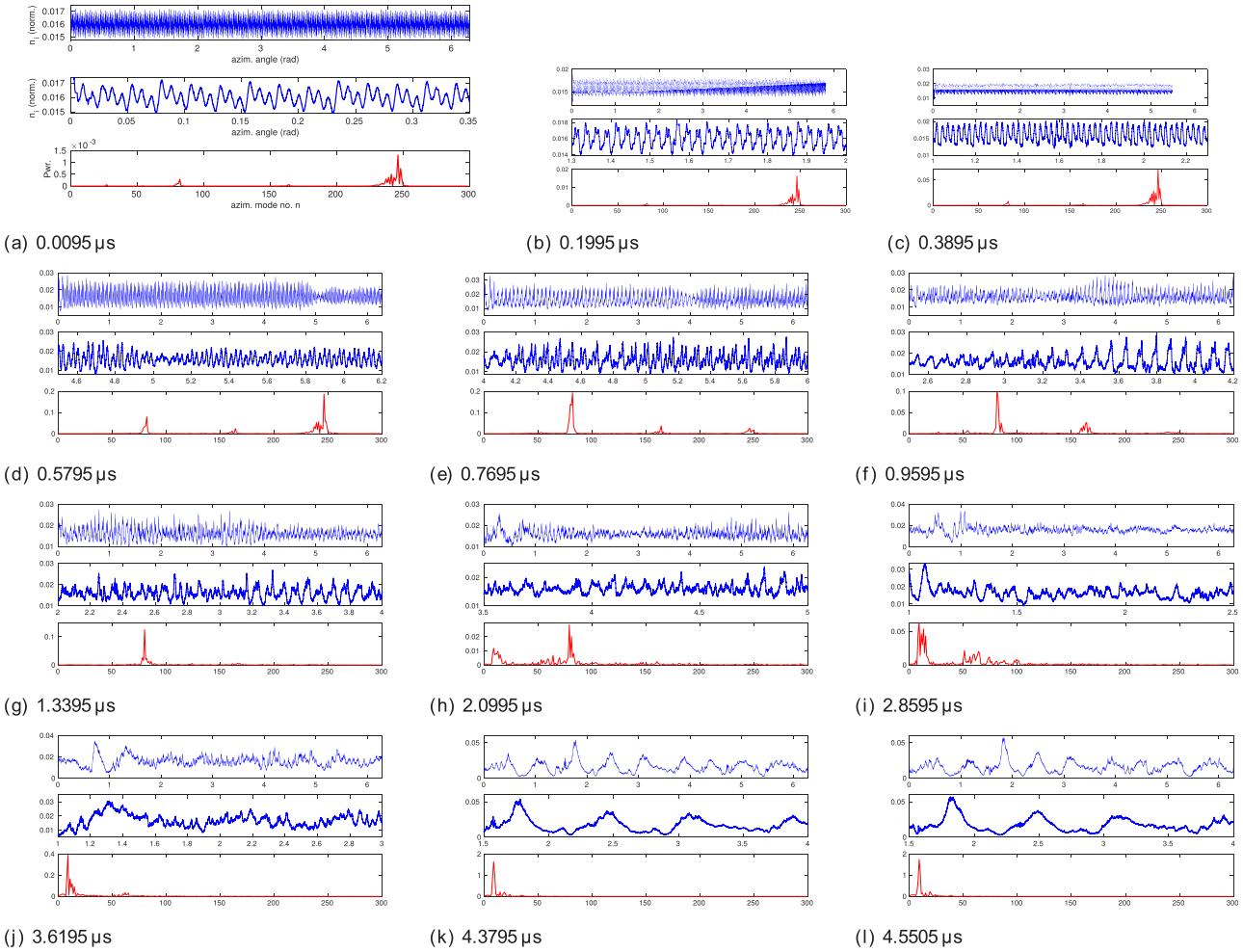

FIG. 10. Xenon plasma: the azimuthal mode structure of the radially averaged Xe^+ density profile is shown at different times. Arbitrary normalization is common for all frames. For each time frame: The top—the radially averaged Xe^+ density function over the full 2π range. The middle—zoomed-in segment of Xe^+ density, showing detailed structure of the azimuthal waveform. The bottom—the azimuthal FFT of the function on the top plot. The x axis of the bottom plot represents the value of the azimuthal mode number, n.

$(n\Omega/\omega_{ce}) = 5$ in the three physically relevant solutions in Fig. 1 are all approximately $\alpha \approx 0.1\omega_{pi} = 3.65 \times 10^6$ rad/s, which agrees well with the observed linear phase growth rate, $\alpha = 3.48 \times 10^6$ rad/s.

Although the linear growth phase is dominated by the $n = 246$ mode, a weak envelope of a $n = 82$ mode is transiently excited during the initial 10 eV ramp up electron temperature [Fig. 10(a)]. Close to the end of the linear evolution, there is a re-emergence of the $n = 82$ mode observed in Fig. 10(d). This is the first sign of nonlinearity in the system. The nonlinear phase commences from Fig. 10(e), with the azimuthal waveform merging in groups of three (see Fig. 8 frame $t = 0.7695\,\mu$s), in an inverse cascade of wave energy from $n = 246$ to $n = 82$. Between $t = 0.0\,\mu$s and $t = 0.7695\,\mu$s [Figs. 10(a)–10(e)], the weakening and disappearance of the $n = 82$, giving way to $n = 246$, followed by the resurgence of the $n = 82$ at the cost of the $n = 246$ can be identified as a form of nonlinear plasma wave recurrence in the system.

The inverse cascade of energy to longer azimuthal wavelengths continues nonlinearly beyond the $n = 82$ in Figs. 10(f)–10(i), taking the azimuthal profile through several transient longer wavelength modes, finally saturating in a stable nonlinear $n = 9$ mode [Figs. 10(k) and 10(l) and frame $t = 4.3795\,\mu$s of Fig. 8].

5. The radial structure of the unstable modes

Radial modes are excited in the nonlinear stage of the EDI. In Fig. 11, the dynamics of radial modes is investigated by first azimuthally averaging the 2D annular Xe^+ density profile, and then scanning the averaged profile for excited radial modes via FFT operation. The time frames analyzed are the same as in Figs. 8 and 10.

Figures 11(a)–11(c) clearly show that in the early linear stage the radial density forms a sharp plateau between the walls, devoid of any internal modes.[31] The first radial wave-structures are formed in the early nonlinear stage of the instability [Figs. 11(e) and 11(f)], and take the form of a $m = 4$ mode. In the late nonlinear stage [Figs. 11(g)–11(l)], the annular profile forms a steep double edged plateau,

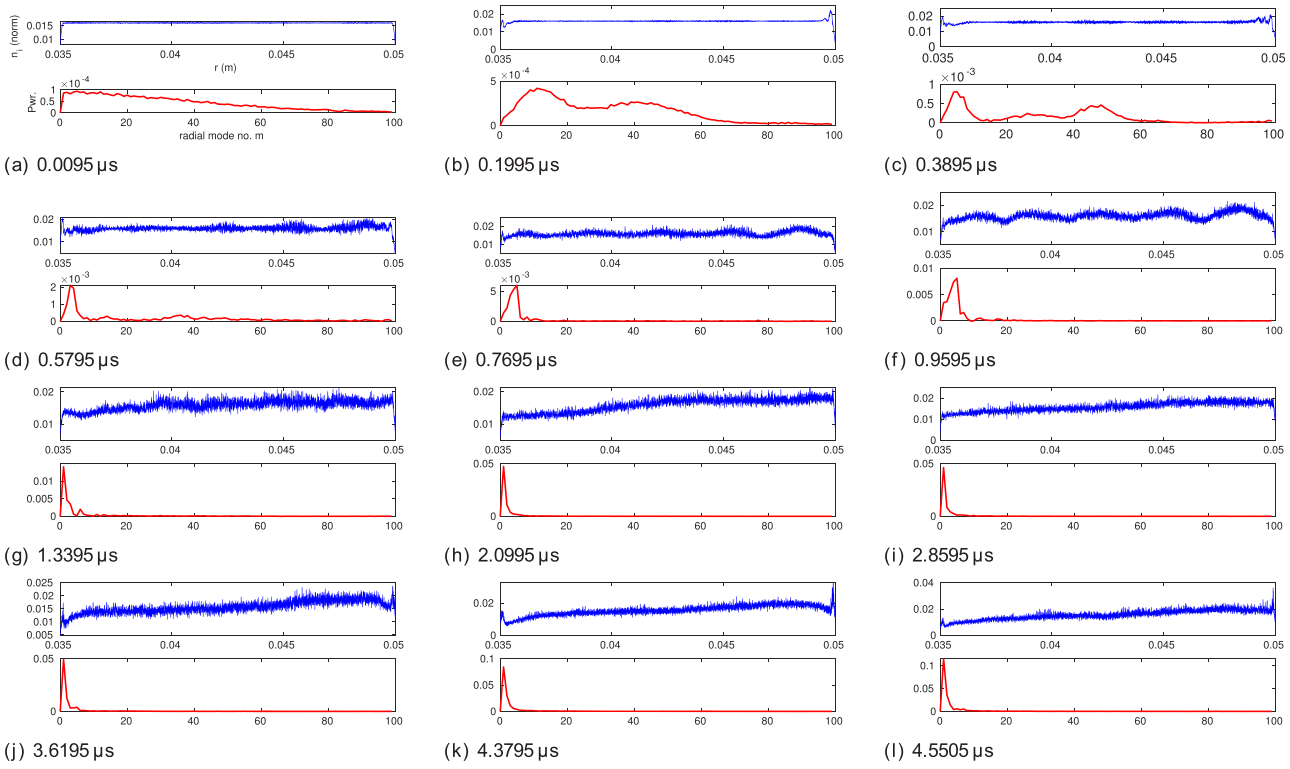

FIG. 11. Xenon plasma: time frames of radial analysis of the azimuthally averaged, Xe^+ density profile with a common arbitrary normalization in all frames. Each time frame has two plots arranged in stack. The top plot is the azimuthally averaged Xe^+ density function between the inner and outer radial walls of the device. The bottom plot is the radial FFT of the function on the top plot. The x axis of the bottom plot represents the value of the radial mode number, m.

with a wide monotonically rising table-top in between. Such a quarter wavelength profile gets registers as a $m = 1$ in the FFT analysis [Figs. 11(g)–11(l)]. It is evident from Figs. 11(g)–11(l), and from the radial shears in the Xe^+ density, in the $t = 4.3795\ \mu s$ frame of Fig. 9, that in the final stages of the instability, the radial plasma profile is strongly shaped by the centrifugal forces acting on the rotating electrons, and ambipolarly on the ions. The saturated profiles [Figs. 11(j)–11(l)] are smooth except for two small peaks very close to the two walls. The single cell width of the peaks suggests that these structures could be the result of a mismatch between the perfect circular boundaries used in the specular reflection operation, and the ragged circular boundaries used in the Cartesian potential solver.

6. Evolution of ions in azimuthal phase space

The time frames in Fig. 12 are the azimuthal angular phase space scatter plots of the xenon ions at different stages of the instability. Note that the range of the x-axes (angular space) in each time frame is different, and adjusted for the best depiction of the corresponding mode in that frame.

Figure 12, frame 0.304 μs is in the linear growth phase (see Fig. 3) with the ion arrangement showing nearly stationary oscillations, matching the wave structure of the $n = 246$ mode. The second frame at 0.684 μs is plotted just after the transition to the longer $n = 82$ mode in the quasi-stationary stage of the instability (see Fig. 3). Here, the first signs of ion trapping and dragging by the wave are observed. Closed loop orbits of ions in the positive velocity space along with a shift in their angular velocity distribution in the positive propagating direction of the $n = 82$ mode indicate that trapped ions are following the wave. Similar closed loop orbits in the ion phase have also been observed in other 1D and 2D EDI simulations.[3,13,20,29] It can be deduced from the 0.684 μs time-frame of Fig. 12 that the ion trapping by the wave causes saturation of the instability in the quasi-stationary stage.

The third and fourth frames of Fig. 12 at 2.204 μs and 3.724 μs are both in the stage of nonlinear transition to the saturated $n = 9$ mode (again refer Fig. 3). The continued presence of the closed loop ion orbits and average ion motion in the direction of wave propagation in these frames indicates that growth of the EDI saturates via the ion trapping mechanism.

B. Modeling EDI using ions species lighter than xenon

1. Argon plasma

The argon plasma potential energy curve in Fig. 3 has a linear phase that lasts only up to 0.34 μs with a growth rate of 6.3×10^6 rad/s. The quasi-stationary phase lasts from 0.34 μs to 1.5 μs, followed by the nonlinear transition and saturation phase from 1.5 μs to the simulation termination at 4.55 μs.

The electron axial mobility of the argon plasma subplot in Fig. 4 shows the same distinct phase transitions as its potential energy curve. The magnitudes of μ_{ez} attained in the first and second saturation is

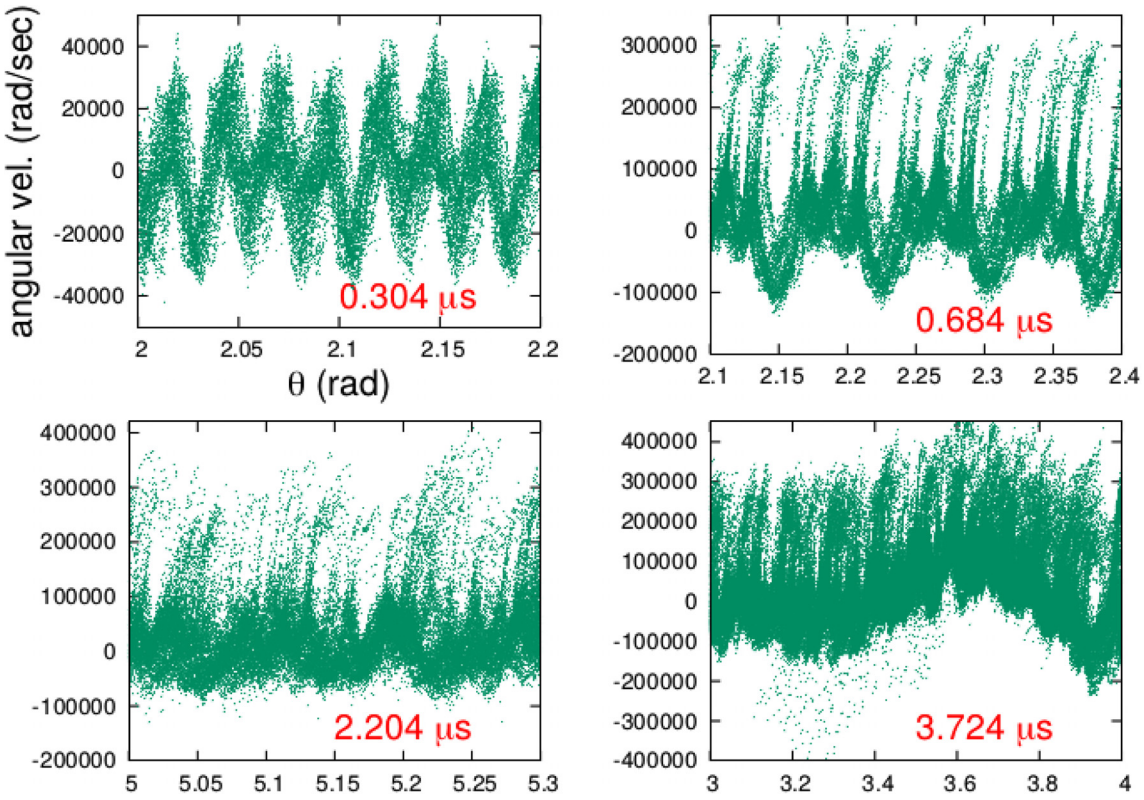

FIG. 12. Xenon plasma: azimuthal phase space structures formed by ions at different stages of the simulation.

very similar to corresponding saturation values in the xenon Plasma simulation (compare argon and xenon subplots of Fig. 4).

In Fig. 6, the subplot for the argon plasma has electron 1D temperatures growing to 25 eV from collisionless heating in the linear growth phase and thereafter stabilizing at this value. The electron temperatures attained from heating by the instability are again comparable to the saturated electron temperatures in the xenon plasma simulation (compare argon and xenon plasma subplots of Fig. 6).

In Fig. 13, the annular Ar^+ profile is plotted at four selected stages of the instability. Of these snapshots, the first one is in the linear growth phase, the second one is in the quasi-stationary energy phase, and the last two are in the nonlinear energy transition and saturation phase. Figure 14 has the azimuthal and radial FFTs of the Ar^+ density profiles depicted in Fig. 13. Visually, it is evident from Figs. 13 and 14 that the dynamics of mode transitions has the same series of events as the Xe^+ thruster, only proceeding at a faster time scale.

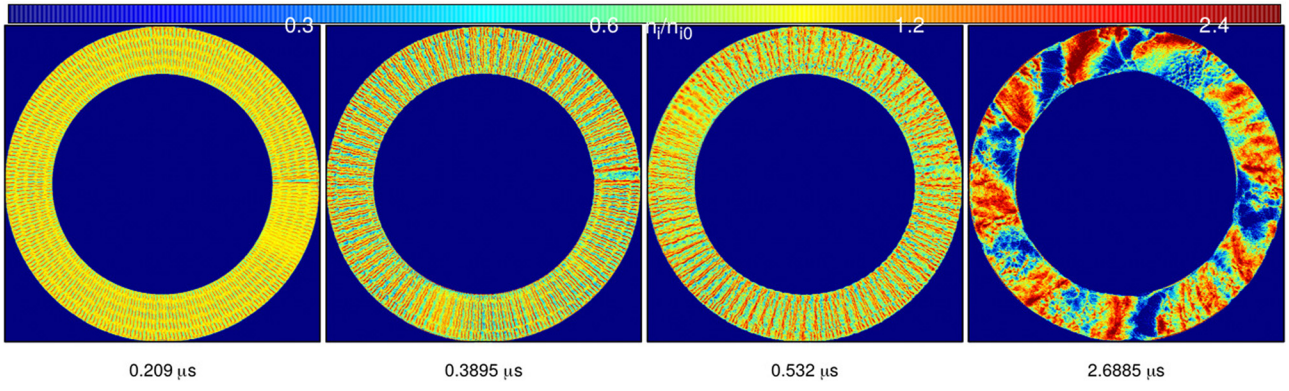

FIG. 13. Argon plasma: selected time-frames of the full annular device showing the evolution of Ar^+ density perturbed by 2D azimuthal-radial modes of EDI. The Ar^+ number density, n_i color bar is logscaled and normalized by its initial value n_{i0}.

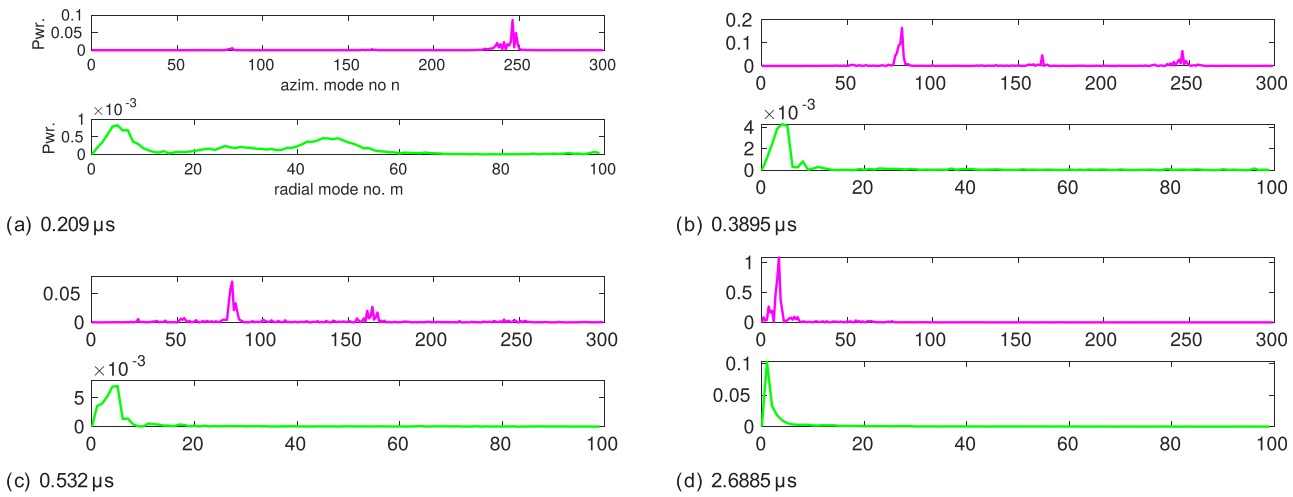

FIG. 14. Argon plasma: azimuthal and radial analysis of the Ar^+ density snapshots of Fig. 13. The x axis for the azimuthal and radial FFT are the azimuthal mode number n and the radial mode number m, respectively.

2. Hydrogen plasma

The hydrogen plasma, by virtue of having the lightest ion component, has the fastest phase transitions of the three experiments. From Fig. 3, it is evident that linear growth of the EDI in the hydrogen plasma at a rate of 5.5×10^7 rad/s lasts only up to 0.04 μs. The following quasi-stationary phase gives way to the nonlinear transition and saturation phase around the 0.35 μs mark. The evolution of the electron axial mobility and electron 1D temperatures in the hydrogen plasma subplots in Figs. 4 and 6, show comparable saturation levels as the xenon and argon plasma simulations.

Figures 15 and 16 are the H^+ density snapshots and their respective mode analysis, wherein time-frames 0.0095 μs and 0.0285 μs are in the linear growth phase, time-frame 0.057 μs is in quasi-stationary phase, and time-frame 4.5505 μs is in the phase of nonlinear transition to saturation. The hydrogen plasma also has the same mode transitions etched in its nonlinear dynamics as the two heavier ion species. Only the EDI evolution happens at a rate that is faster by an order of magnitude, compared to the xenon or argon ion plasma.

3. EDI scaling with ion mass

It has already been emphasized that the linear growth and nonlinear inverse cascade of the EDI modes in the three simulations evolve through the same set of stable and unstable mode configurations at different time-scales. Other interesting comparative aspects are—(i) there is a $(m_i/m_e)^{-0.6}$ power law scaling of the linear phase growth rate as a function of ion mass (inset of Fig. 3), (ii) rate of electron heating by the instability follows the same power law scaling with ion mass, but the final electron temperature attained is around 25 eV irrespective of ion mass (Fig. 6), and (iii) the electron axial mobility evolves at different time-scales within the same range of values in the three experiments (Fig. 4). Hence, from the perspective EDI mode

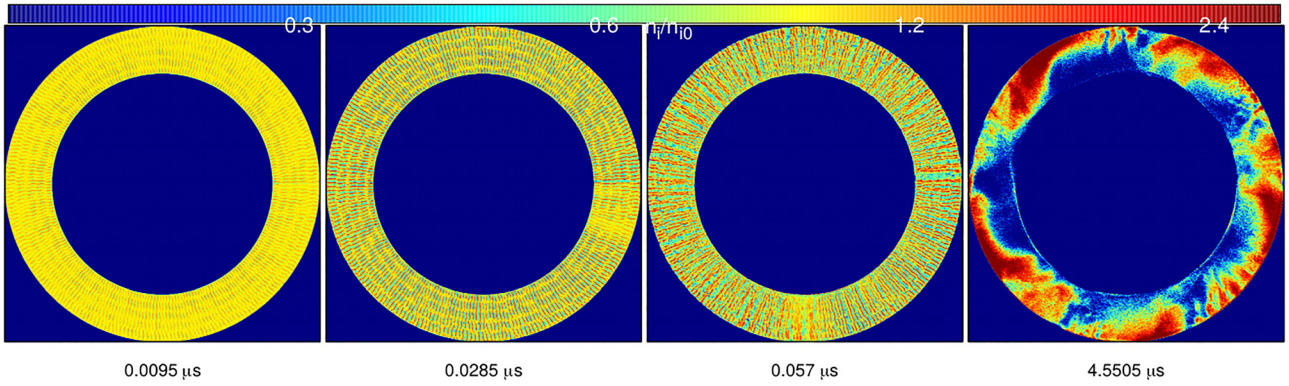

FIG. 15. Hydrogen plasma: selected time-frames of the full annular device showing the evolution of H^+ density perturbed by 2D azimuthal-radial modes of EDI. The H^+ number density, n_i color bar is logscaled and normalized by its initial value n_{i0}.

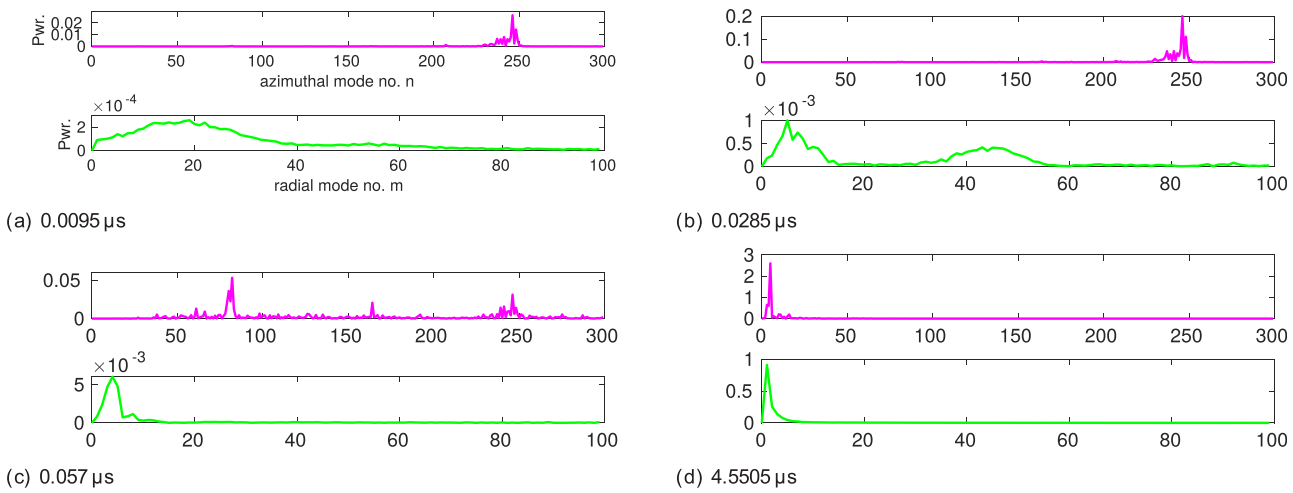

FIG. 16. Hydrogen plasma: azimuthal and radial analysis of the H^+ density snapshots of Fig. 15. The x axis for the azimuthal and radial FFT are the azimuthal mode number n and the radial mode number m, respectively.

transitions, electron heating, and electron transport, there is a smooth scaling of the collisionless plasma dynamics with ion mass.

4. Hydrogen plasma simulation in half-sized annular device

The fast saturation of the instability in hydrogen plasma makes this plasma well suited for test simulations verifying hypotheses and numerical convergence studies.

One such test is performed to study how azimuthal domain size influences the inverse cascade process and the saturation at long wavelengths. This is done by simulating the hydrogen plasma in a smaller annular device of 5 cm diameter that is half the diameter of the original device. Other parameters such as loaded plasma density, net computational particles used, total number of cells in the simulation domain, the virtual axial length, the cold loading and re-injection, the magnetic field at the inner radial wall, and the aspect ratio of the annular channel are kept unchanged. As the device is shrunk to half-size, the radial width of the channel is also halved but since the aspect ratio is unchanged the magnetic field falls by the same value from the inner radial wall to the outer radial wall, albeit along a sharper curve.

Figure 17 shows a comparison of the electron axial mobility and its time average in the full sized (10 cm) device and the half-sized (5 cm) device. The mobility comparisons show that on an average the electron anomalous mobility in the half-sized device is (2/3)rd of that in the full sized device.

Furthermore, the azimuthal wave structure of the saturated mode at 0.751 μs is compared between the two devices in Fig. 18. The azimuthal domain is laid out at the respective mean radii of the two devices, and the wave structure of the H^+ density function is plotted. The azimuthal length shown in Fig. 18 is nearly the full $2\pi\,rad$ angular domain of the 5 cm device and half the angular domain of the 10 cm device. The H^+ density wave-function of the 10 cm device is truncated to the domain length shown in Fig. 18. It is seen that this domain size

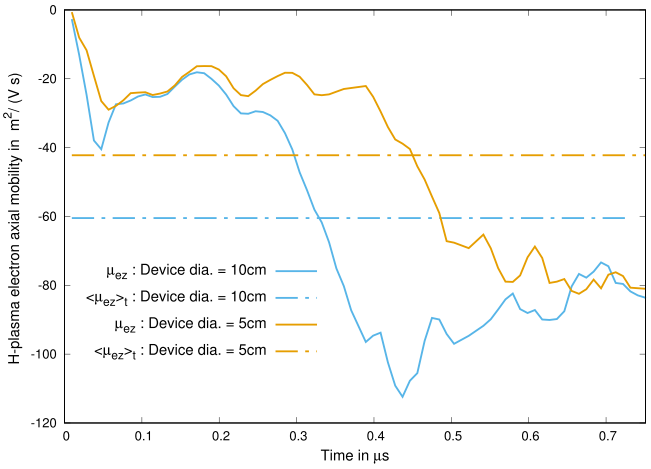

FIG. 17. Hydrogen plasma: comparison of the electron axial mobility evolution between the 10 cm annular device and a smaller 5 cm annular device. Here, $\langle \mu_{ez} \rangle_t$ is the time average of μ_{ez} in the time period of 0.751 μs plotted.

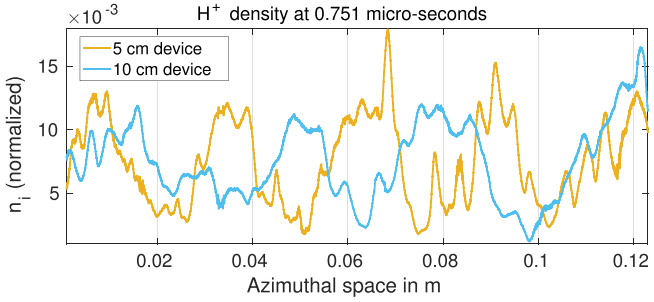

FIG. 18. Hydrogen plasma: comparison of the saturated, radially averaged ion density function at 0.751 μs between the 10 cm and 5 cm device simulations. The 12.3 cm range on x axis represents full azimuthal domain of the 5 cm device and half azimuthal domain of the 10 cm device. The density function of the 10 cm device is truncated to fit the domain.

accommodates five peaks of the saturated mode in the half-size device, and only four peaks of the saturated mode in the full-size device.

Figures 15 and 16 indicate that in longer azimuthal domains modes inversely cascade to longer wavelengths, generating greater anomalous electron transport. The finding supports the earlier hypothesis on why observed anomalous electron mobility from annular device simulation is greater than that obtained from Cartesian box simulations with periodic azimuthal domains.

Another outcome of this test simulation is that in the linear phase when the mode length scale (1 mm) is too small to be affected by the system size, it serves as the numerical convergence test performed with a twice finer mesh ($\Delta x = 0.07$ mm) that is shorter than the Debye length ($\lambda_D = 0.074$ mm) at the linear phase temperature of 10 eV. From Fig. 17, it is evident that the growth rate, first transition point, and anomalous electron transport in the linear phase are very similar in the two devices. In fact, the μ_{ez} curves of the two devices essentially start diverging in the nonlinear stage when the inverse cascade of modes sets in. The matching linear phase results between the $\Delta x = 0.07$ mm mesh and the $\Delta x = 0.14$ mm indicate that the main simulations on the larger mesh are not significantly deviated by the numerical grid heating. As explained in Sec. III, it is the cold re-injection of electrons in the virtual axial domain that controls the electron heating in the system.

5. Convergence tests using a higher particles-per-cell (ppc) number

A set of convergence tests have been conducted with higher particles per cell (ppc = 30, 60) to check if the results are numerically sensitive to the particle representation number. Again hydrogen plasma has been chosen as it has the fastest evolution. In Fig. 19, the electrostatic energy curves for ppc = 13, 30, and 60 have been plotted. The overall shapes and magnitudes of the three curves are consistent with a slight divergence in the nonlinear transition to saturation phase. The emergence of the divergence in the late stage raises the question whether this divergence is a result of the progression of the instability or other (numerical) issues. Further tests have been conducted with argon plasma taking ppc = 13, 60. These are also plotted in Fig. 19 and should be compared with the corresponding linear phase H-plasma plots in the inset. The curves indicate that the level of convergence in the three stages is similar for all ion species. Other diagnostics compared between the ppc = 13 and pp = 60 H-plasma simulations include the measured electron axial mobilities (Fig. 20) and the mode structures formed through inverse cascade at $t = 0.371\ \mu$s (Fig. 21). Both Figs. 20 and 21 demonstrate fair convergence in their respective diagnostic.

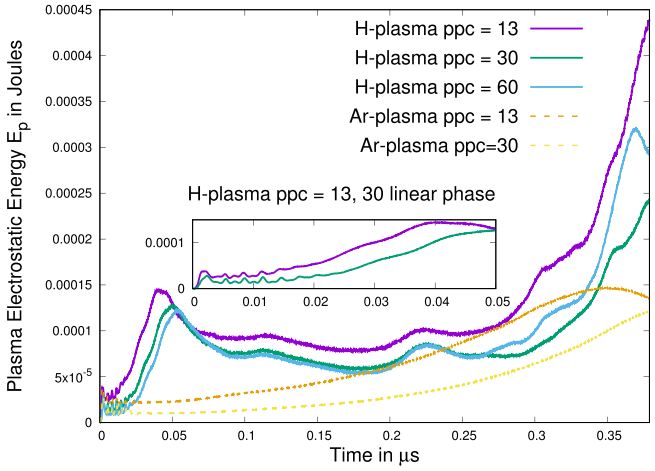

FIG. 19. Convergence test: comparison of the plasma electrostatic energy, E_p evolution in H-plamsa experiments performed using 13, 30, and 60 particles-per-cell (ppc). On the same graph Ar-plasma E_p is compared between simulations having ppc =13 and 60. (Inset): the linear phase of the H-plasma E_p curves for ppc = 13, 60 are zoomed in for comparison with the Ar-plasma E_p curves.

V. CONCLUSIONS AND DISCUSSION

2D3V PIC simulation has been used to model the azimuthal-radial dynamics of the Electron Drift Instability in a Hall thruster of 10 cm diameter. The novel aspects of this numerical set-up are—(a) conducting the experiment on the full 2π azimuthal domain of the annular thruster channel including radially inhomogeneous magnetic field and (b) simulating effects of the device curvature such as centrifugal forces on rotating electrons.

The results indicate the importance of full scale simulations with realistic azimuthal dimension. It is demonstrated that use of the complete azimuthal domain of the 10 cm device allows nonlinear transitions of modes to longer wavelengths, and generates more anomalous electron transport, compared to simulations in smaller, periodic azimuthal domains. The centrifugal force on the rotating electrons also influences the radial mode structure by developing a radially rising plasma density profile in the stationary state of the instability.

Several interesting aspects of the mode dynamics also emerge from the simulations. A linear excitation of the electron drift instability results in a short scale azimuthal mode, $n = 246$ that grows linearly in amplitude accompanied by the electron heating and enhanced axial transport. The linear growth phase transitions into a nonlinear quasi-stationary stage with longer wavelength of the azimuthal modes. This quasi-stationary stage is followed by yet another nonlinear transition to a saturated energy stage, in which longer wavelength corresponding

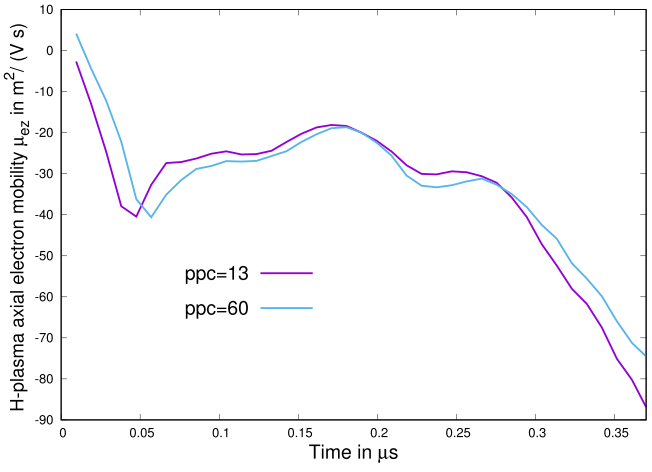

FIG. 20. Convergence test: comparison of the electron axial mobility, μ_{ez} evolution in H-plasma experiments performed with ppc = 13 and 60.

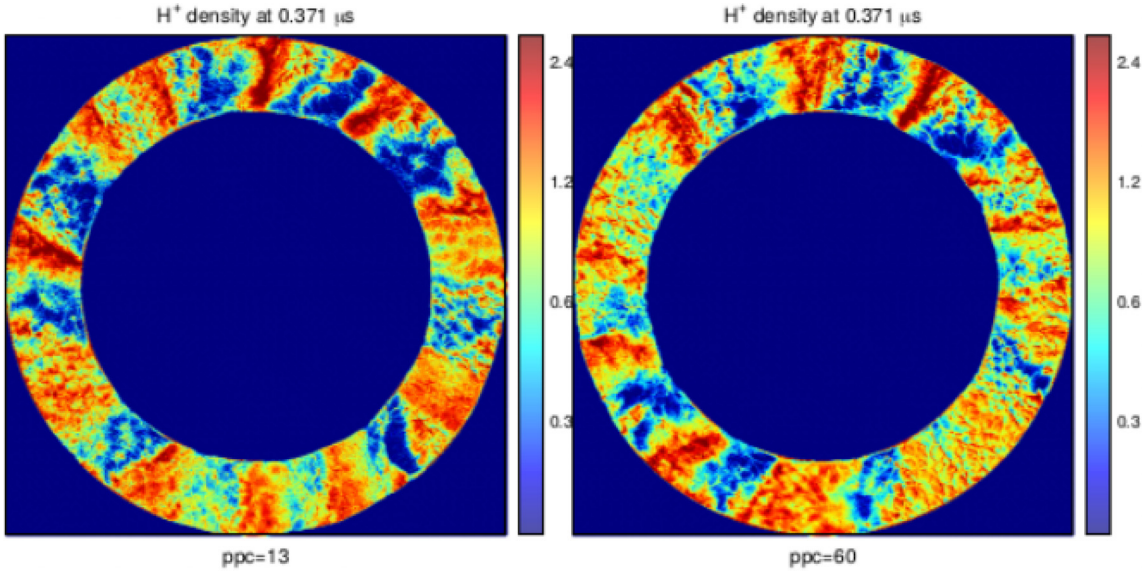

FIG. 21. Convergence test: comparison of the H^+ density distribution at $t = 0.371$ μs between the ppc = 13 and 60 experiments.

to a $n = 9$ mode is observed on the annular profile, similar to rotating spoke-like structures.[21,53,58] For the Xe-plasma with long wavelength, spoke structures propagate at an average rotation frequency of 3.368×10^5 rad/s, which is two orders slower than the rigid angular drift velocity of the electrons.

It is revealed by azimuthal phase space scatter plots of the ions that a fraction of the ions that initially perform stationary oscillations in the field structure of the azimuthal wave are eventually trapped and dragged along by the wave in the nonlinear stages, leading to saturation of the instability.

The radial profile remains a flat plateau between the walls in the linear stage of the instability followed by the excitation of shorter length scale radial modes, $m = 4$ observed in the nonlinear stage, similar to Ref. 51. The radial modes follow a similar, but comparatively more phase-mixed, transition to longer length scales. The radial profile that emerges in the saturation phase is a quarter wavelength function rising toward the outer wall, a signature of the inherent centrifugal forces on rotating electrons affecting the plasma profile and nonlinear dynamics.[59]

The transitions in the anomalous axial electron mobility are strongly correlated with the wave energy (see Figs. 3 and 4). The mobility is much larger than Bohm mobility and gets enhanced by the inverse cascade of the azimuthal modes.

Scaling of the EDI with ion mass has been investigated by conducting the numerical experiment with xenon, argon, and hydrogen plasmas. The linear growth of EDI scales with the ion mass in the form of the power law $(m_i/m_e)^{-0.6}$. The nonlinear transitions in the wave structure, anomalous mobility, and electron temperature occur in similar patterns for different ion masses, albeit with longer time-scales for heavier ions, as generally expected.

ACKNOWLEDGMENTS

This work was carried out under grants from NSERC Canada and the U.S. Air Force Office of Scientific Research No. FA9550-15-1-0226. Computational resources were provided by Westgrid/Compute Canada and the Plato cluster at the University of Saskatchewan. A.S. acknowledges the useful discussions with Y. Raitses and I. Kaganovich, as well as participants of the 2018 E × B Worskhop at Princeton University. M.S. thanks L. Coudel and T. Zintel for Linux and cluster related help, and O. Chapurin and S. Janhunen (University of Texas, USA) for their python based dispersion solver used in the analytical solutions of this paper. The authors thank the anonymous referees for valuable suggestions on this work.

REFERENCES

[1]S. P. Gary and J. J. Sanderson, J. Plasma Phys. **4**, 739 (1970).
[2]D. W. Forslund, R. L. Morse, and C. W. Nielson, Phys. Rev. Lett. **25**, 1266 (1970).
[3]J.-P. Boeuf, J. Appl. Phys. **121**, 011101 (2017).
[4]M. Cappelli, Phys. Today **62**(4), 76 (2009).
[5]C. L. Ellison, Y. Raitses, and N. J. Fisch, Phys. Plasmas **19**, 013503 (2012).
[6]S. N. Abolmasov, Plasma Sources Sci. Technol. **21**, 035006 (2012).
[7]J. P. Boeuf, J. Claustre, B. Chaudhury, and G. Fubiani, Phys. Plasmas **19**, 113510 (2012).
[8]A. T. Powis, J. A. Carlsson, I. D. Kaganovich, Y. Raitses, and A. Smolyakov, Phys. Plasmas **25**, 072110 (2018).
[9]E. Rodríguez, V. Skoutnev, Y. Raitses, A. Powis, I. Kaganovich, and A. Smolyakov, Phys. Plasmas **26**, 053503 (2019).
[10]A. M. DuBois, E. Thomas, Jr., W. E. Amatucci, and G. Ganguli, Phys. Plasmas **21**, 062117 (2014).
[11]L. Muschietti and B. Lembège, J. Geophys. Res.: Space Phys. **118**, 2267, https://doi.org/10.1002/jgra.50224 (2013).
[12]M. E. Koepke, W. E. Amatucci, J. J. Carroll, and T. E. Sheridan, Phys. Rev. Lett. **72**, 3355 (1994).
[13]T. Lafleur, S. D. Baalrud, and P. Chabert, Phys. Plasmas **23**, 053502 (2016).
[14]T. Lafleur, S. D. Baalrud, and P. Chabert, Phys. Plasmas **23**, 053503 (2016).
[15]A. Simon, Phys. Fluids **6**, 382 (1963).
[16]F. C. Hoh, Phys. Fluids **6**, 1184 (1963).
[17]K. I. Thomassen, Phys. Fluids **9**, 1836 (1966).
[18]R. C. Davidson and H. Uhm, Phys. Fluids **20**, 1938 (1977).

[19]M. Sengupta and R. Ganesh, Phys. Plasmas **22**, 072112 (2015).
[20]T. Lafleur and P. Chabert, Plasma Sources Sci. Technol. **27**, 015003 (2017).
[21]K. Matyash, R. Schneider, S. Mazouffre, S. Tsikata, and L. Grimaud, Plasma Sources Sci. Technol. **28**, 044002 (2019).
[22]A. I. Smolyakov, O. Chapurin, W. Frias, O. Koshkarov, I. Romadanov, T. Tang, M. Umansky, Y. Raitses, I. D. Kaganovich, and V. P. Lakhin, Plasma Phys. Controlled Fusion **59**, 014041 (2017).
[23]T. Lafleur, R. Martorelli, P. Chabert, and A. Bourdon, Phys. Plasmas **25**, 061202 (2018).
[24]J. C. Adam, A. Héron, and G. Laval, Phys. Plasmas **11**, 295 (2004).
[25]A. Ducrocq, J. C. Adam, A. Héron, and G. Laval, Phys. Plasmas **13**, 102111 (2006).
[26]S. Janhunen, A. Smolyakov, O. Chapurin, D. Sydorenko, I. Kaganovich, and Y. Raitse, Phys. Plasmas **25**, 011608 (2018).
[27]S. Janhunen, A. Smolyakov, D. Sydorenko, M. Jimenez, I. Kaganovich, and Y. Raitse, Phys. Plasmas **25**, 082308 (2018).
[28]P. Coche and L. Garrigues, Phys. Plasmas **21**, 023503 (2014).
[29]V. Croes, T. Lafleur, Z. Bonaventura, A. Bourdon, and P. Chabert, Plasma Sources Sci. Technol. **26**, 034001 (2017).
[30]A. Héron and J. C. Adam, Phys. Plasmas **20**, 082313 (2013).
[31]F. Taccogna and P. Minelli, Phys. Plasmas **25**, 061208 (2018).
[32]K. Hara and S. Cho, "Radial-azimuthal particle-in-cell simulation of a Hall effect thruster," in 35th International Electric Propulsion Conference, IEPC Paper 2017-495, Atlanta, GA, October (2017).
[33]M. Lampe, J. B. McBride, W. Manheimer, R. N. Sudan, R. Shanny, J. H. Orens, and K. Papadopolous, Phys. Fluids **15**, 662 (1972).
[34]J. Cavalier, N. Lemoine, G. Bonhomme, S. Tsikata, C. Honoré, and D. Grésillon, Phys. Plasmas **20**, 082107 (2013).
[35]O. Koshkarov and A. Smolyakov, Phys. Rev. Lett. **122**, 185001 (2019).
[36]M. J. Sekerak, A. D. Gallimore, D. L. Brown, R. R. Hofer, and J. E. Polk, J. Propul. Power **32**, 903 (2016).
[37]Z. A. Brown and B. A. Jorns, Phys. Plasmas **26**, 113504 (2019).
[38]L. B. King, paper presented at the 29th International Electric Propulsion Conference, Princeton University, October 31–November 4 (IEPC, 2005).
[39]V. I. Arefev, Sov. Phys. Tech. Phys.-USSR **14**, 1487 (1970).
[40]O. Buneman, J. Nucl. Energy, Part C: Plasma Phys. **4**, 111 (1962).
[41]J. B. McBride, E. Ott, J. P. Boris, and J. H. Orens, Phys. Fluids **15**, 2367 (1972).
[42]M. Sengupta, "Studies in non-neutral plasmas using particle-in-cell simulations," Ph.D. thesis (HBNI, 2017).
[43]C. K. Birdsall and A. B. Langdon, *Plasma Physics via Computer Simulation* (Taylor and Francis Group, 2004).
[44]D. P. Kroese, T. Taimre, and Z. I. Botev, *Handbook of Monte Carlo Methods* (Wiley, 2011), pp. 29–31.
[45]S. A. Chin, Phys. Rev. E **77**, 066401 (2008).
[46]M. Sengupta and R. Ganesh, Phys. Plasmas **21**, 022116 (2014).
[47]M. Sengupta and R. Ganesh, AIP Conf. Proc. **1668**, 020005 (2015).
[48]M. Sengupta and R. Ganesh, Phys. Plasmas **23**, 102111 (2016).
[49]M. Sengupta and R. Ganesh, Phys. Plasmas **24**, 032105 (2017).
[50]J.-P. Boeuf, Front. Phys. **2**, 74 (2014).
[51]F. Taccogna, P. Minelli1, Z. Asadi, and G. Bogopolsky, Plasma Sources Sci. Technol. **28**, 064002 (2019).
[52]E. T. Dale and B. A. Jorns, Phys. Plasmas **26**, 013516 (2019).
[53]J. P. Boeuf, Phys. Plasmas **26**, 072113 (2019).
[54]B. M. Reid, "The influence of neutral flow rate in the operation of hall thrusters," Ph.D. thesis (University of Michigan, 2009).
[55]M. S. McDonald, "Electron transport in hall thrusters," Ph.D. thesis (University of Michigan, 2012).
[56]M. K. Allis, N. Gascon, E. Fernandez, C. Vialard-Goudou, and M. Cappelli, in AIAA Meeting Paper 40th AIAA/ASME/SAE/ASEE Joint Propulsion Conference and Exhibit 2004, AIAA Paper No. 2004 3951 (2012).
[57]M. A. Cappelli, C. V. Young, E. Cha, and E. Fernandez, Phys. Plasmas **22**, 114505 (2015).
[58]J.-P. Boeuf and B. Chaudhury, Phys. Rev. Lett. **111**, 155005 (2013).
[59]A. Domínguez-Vázquez, F. Taccogna, and E. Ahedo, Plasma Sources Sci. Technol. **27**, 064006 (2018).